Experimental Neurology 365 (2023) 114429

Contents lists available at ScienceDirect

Experimental Neurology

journal homepage: www.elsevier.com/locate/yexnr

Research paper

POLG genotype influences degree of mitochondrial dysfunction in iPSC derived neural progenitors, but not the parent iPSC or derived glia

Yu Hong [a,b], Cecilie Katrin Kristiansen [a,b], Anbin Chen [a,c], Gonzalo Sanchez Nido [a,b], Lena Elise Høyland [d], Mathias Ziegler [d], Gareth John Sullivan [e,f,g,h], Laurence A. Bindoff [a,i], Kristina Xiao Liang [a,b,*]

[a] Department of Clinical Medicine (K1), University of Bergen, Jonas Lies vei 87, P. O. Box 7804, 5021 Bergen, Norway
[b] Neuro-SysMed, Center of Excellence for Clinical Research in Neurological Diseases, Haukeland University Hospital, Jonas Lies vei 87, P. O. Box 7804, 5021 Bergen, Norway
[c] Department of Neurosurgery, Xinhua Hospital Affiliated to Shanghai Jiaotong University School of Medicine, Shanghai 200092, China
[d] Department of Biomedicine, University of Bergen, Jonas Lies Vei 91, 5009 Bergen, Norway
[e] Department of Molecular Medicine, Institute of Basic Medical Sciences, University of Oslo, P. O. Box 1105, Blindern, 0317 Oslo, Norway
[f] Institute of Immunology, Oslo University Hospital, PO Box 4950, 0424 Oslo, Norway
[g] Hybrid Technology Hub Centre of Excellence, Institute of Basic Medical Sciences, University of Oslo, P. O. Box 1110, Blindern, 0317 Oslo, Norway
[h] Department of Pediatric Research, Oslo University Hospital, P. O. Box 4950, Nydalen, 0424 Oslo, Norway
[i] Department of Neurology, Haukeland University Hospital, Jonas Lies vei 87, P. O. Box 7804, 5021 Bergen, Norway

ARTICLE INFO

Keywords:
POLG
Mitochondrial function
Genotype
Neural stem cells
Neuron

ABSTRACT

Diseases caused by *POLG* mutations are the most common form of mitochondrial diseases and associated with phenotypes of varying severity. Clinical studies have shown that patients with compound heterozygous *POLG* mutations have a lower survival rate than patients with homozygous mutations, but the molecular mechanisms behind this remain unexplored. Using an induced pluripotent stem cell (iPSC) model, we investigate differences between homozygous and compound heterozygous genotypes in different cell types, including patient-specific fibroblasts, iPSCs, and iPSC-derived neural stem cells (NSCs) and astrocytes. We found that compound heterozygous lines exhibited greater impairment of mitochondrial function in NSCs than homozygous NSCs, but not in fibroblasts, iPSCs, or astrocytes. Compared with homozygous NSCs, compound heterozygous NSCs exhibited more severe functional defects, including reduced ATP production, loss of mitochondrial DNA (mtDNA) copy number and complex I expression, disturbance of NAD^+ metabolism, and higher ROS levels, which further led to cellular senescence and activation of mitophagy. RNA sequencing analysis revealed greater downregulation of mitochondrial and metabolic pathways, including the citric acid cycle and oxidative phosphorylation, in compound heterozygous NSCs. Our iPSC-based disease model can be widely used to understand the genotype-phenotype relationship of affected brain cells in mitochondrial diseases, and further drug discovery applications.

1. Introduction

Human mtDNA is replicated and repaired by polymerase gamma, Pol γ. Human Pol γ is composed of three subunits encoded by two nuclear genes: *POLG* gene codes for the 140-kilodalton (kDa) catalytic subunit, p140 and *POLG2* encodes the ~110-kDa homodimeric accessory subunit, p55. The *POLG* gene encodes the enzyme synthesizing the mtDNA and correcting mtDNA errors. Mutations in *POLG* gene are the most common causes of inherited mitochondrial diseases and POLG-related disorders comprise a continuum of overlapping phenotypes with onset

Abbreviations: iPSC, induced pluripotent stem cell; NSC, neural stem cell; mtDNA, mitochondrial DNA; DA, dopaminergic; MMP, mitochondrial membrane potential; ROS, reactive oxygen species; ESC, embryonic stem cell; DE, differential expression; Human-GEM, human genome-scale metabolic model; MTG, MitoTracker Green; TMRE, tetramethylrhodamine ethyl ester; DCFDA, 2′, 7′- dichlorodihydrofluorescein diacetate; MTDR, MitoTracker Deep Red; PCA, principal component analysis; LC-MS, liquid chromatography mass spectrometry; SIRT1, Sirtuin 1; p-SIRT1, phosphorylated SIRT1; DCX, doublecortin; GS, glutamine synthesis; UCP2, uncoupling protein 2; CPM, counts per million; PFA, paraformaldehyde.

* Corresponding author at: Department of Clinical Medicine (K1), University of Bergen, Jonas Lies vei 87, P. O. Box 7804, 5021 Bergen, Norway.
E-mail address: xiao.liang@uib.no (K.X. Liang).

https://doi.org/10.1016/j.expneurol.2023.114429
Received 29 January 2023; Received in revised form 12 March 2023; Accepted 21 April 2023
Available online 25 April 2023

from infancy to late adulthood. Mitochondrial dysfunction has also been implicated in the pathophysiology of common forms of neurodegeneration such as Parkinson's disease, therefore, studying how *POLG* mutations affect mitochondrial function and cellular homeostasis is relevant to a variety of neurodegenerative diseases.

POLG is one of several nuclear genes that are associated with mtDNA depletion or multiple deletion disorder (Rahman and Copeland, 2019), but while mutations in *POLG* can affect the quality or quantity of mtDNA, the type of mtDNA defect depends on the tissue affected in the brain (Tzoulis et al., 2014a; Tzoulis et al., 2013). For example, we have shown that severe mtDNA depletion is present in neurons from a very early age, even before morphological changes appear, while mtDNA deletions and point mutations show time-dependent accumulation (Tzoulis et al., 2014a).

To date, more than 300 different pathogenic mutations of *POLG* gene have been identified (Rahman and Copeland, 2019). Among them, c.2243G > C (p.W748S) and c.1399G > A (p.A467T) are two founder mutations. Our previous clinical studies suggested that compound heterozygous patients (W748S/A467T) manifested a more severe phenotype than homozygous A467T or W748S (Tzoulis et al., 2006a). However, their genotype-phenotype differences and underlying mechanisms have remained unclear, in part due to the lack of accurate and appropriate models. Human iPSC technology allows the modeling of human disease in a reproducible and tissue-specific manner without the need for animal models or the use of human material obtained through biopsy or postmortem. We have used this technology to perform molecular studies of the pathogenesis of POLG-related diseases (Liang et al., 2020a; Chen et al., 2022; Chen et al., 2021; Liang et al., 2020b; Liang et al., 2021a).

We previously generated human iPSCs from two POLG patients, one carrying W748S/W748S homozygote ($POLG^{homo}$) and the other harboring compound heterozygous for A467T/W748S ($POLG^{comp}$). Using these lines, we generated NSCs and dopaminergic (DA) neurons (Liang et al., 2021a; Liang et al., 2020c) and showed that they displayed a phenotype that faithfully replicated the molecular and biochemical changes found in postmortem brain tissue of patients (Liang et al., 2020c). Further, we compared these POLG iPSC-derived neuronal cells with healthy controls and found that both $POLG^{homo}$ and $POLG^{comp}$ neuronal cells showed distinct mitochondrial defects, including reduced mitochondrial membrane potential (MMP), ATP depletion, mtDNA depletion, complex I loss, and aberrant NAD^+ metabolism (Liang et al., 2021a; Liang et al., 2020c).

In this study, we compared $POLG^{homo}$ and $POLG^{comp}$ cells and analyzed how these genotypes behaved in different cell lineages. We investigated mitochondrial function including MMP, respiratory chain complexes, reactive oxygen species (ROS) and mtDNA copy number in fibroblasts, iPSCs, neuronal cells and astrocytes. In addition, we investigated the transcriptome in cells with phenotypic differences to understand the different impact these genotypes had on other pathways. We found that mitochondrial dysfunction and metabolic pathway dysregulation were more severe in compound heterozygote, but only in neuronal cells and not in fibroblasts, iPSCs or astrocytes.

2. Results

2.1. Compound heterozygous patients have a worse prognosis than those with homozygous mutations

We showed previously that compound heterozygous $POLG^{comp}$ patients had a poorer prognosis than $POLG^{homo}$ patients (Tzoulis et al., 2006b). To confirm this, we expanded the sample size by systematically reviewing studies involving patients with both genotypes in Norway, Finland, the UK, Belgium and Sweden (Table S1). We reviewed five published articles (Tzoulis et al., 2006b; Hakonen et al., 2005; Lax et al., 2012; Janssen et al., 2016; Kollberg et al., 2006) and analyzed a total of 50 patients, of which 14 were $POLG^{comp}$ patients (7 in Norway, 2 in United Kingdom, 3 in Belgium and 2 in Sweden) and 36 $POLG^{homo}$ patients (13 in Norway, 19 in Finland, 2 in Belgium and 2 in Sweden). Median survival time analysis showed that $POLG^{comp}$ patients (9 years) had significantly ($P = 0.007$) lower survival than $POLG^{homo}$ patients (42 years, Fig. S1) confirming our previous observation (Tzoulis et al., 2006b).

2.2. Mitochondrial metabolic pathways are dysregulated in POLG NSCs

IPSCs were reprogrammed from patient fibroblasts using a viral system. We generated NSCs from patient iPSCs via a dual SMAD inhibition approach (Fig. 1A), as described previously (Liang et al., 2020c). All iPSCs exhibited typical ESC morphology with sharp edges, however, $POLG^{comp}$ iPSCs exhibited looser packing cells and larger cell size than $POLG^{homo}$ clones (Fig. 1B). Flow cytometry analysis showed that all iPSC lines had over 99% of cells stained with the pluripotent stem cell marker OCT4 and SSEA4 (Fig. 1C). Immunostaining confirmed that both $POLG^{homo}$ (Figure1D) and $POLG^{comp}$ iPSCs (Fig. 1E) expressed the specific pluripotent marker OCT4, SOX2 and NANOG. We characterized iPSC derived NSCs using immunostaining for the neural stem cell marker PAX6 and NETSIN and found the NSCs showed positive staining for both markers (Fig. 1F). Age-matched iPSC controls and two human embryonic stem cell lines (ESCs): ESC 429 and H1, were used as disease-free controls. To minimize phenotypic diversity caused by intraclonal variation, multiple iPSC clones were included.

Next, we combined the two genotypes into one patient group and all control lines into one control group, and then compared the transcriptomes of iPSCs and their NSCs derived from POLG patients and controls. Sample correlation analysis revealed clear differences between NSC and iPSC/ESC cell types, as well as between the different $POLG^{homo}$ and $POLG^{comp}$ genotypes in each cell type (Fig. 2A). Differential expression (DE) analysis of iPSCs and NSCs showed that the number of DE genes in NSCs was much higher than in iPSCs: 1295 upregulated genes and 1263 downregulated genes in patient iPSCs versus control iPSCs, whereas there were 3452 upregulated genes and 3128 downregulated genes in patient NSCs compared to control NSCs (Fig. 2B). KEGG module pathway analysis of DE genes revealed that patient NSCs exhibited downregulated mitochondrial oxidative phosphorylation-related pathways, including F- and V-type ATPases, citrate cycle enzymes, NADH dehydrogenase, and cytochrome *c* oxidation compared with controls (Fig. 2C). In contrast, no significantly enriched metabolic pathways were found in patient iPSCs compared to controls.

Further, we constructed a genome-scale metabolic model of iPSCs and NSCs based on the mRNA expression status of control iPSCs/ESCs and NSCs using the public human genome-scale metabolic model (Human-GEM) (Robinson et al., 2020). The constructed metabolic model included 7629 reactions, 6342 metabolites, and 2685 genes in iPSCs, and 6877 reactions, 5493 metabolites, and 2594 genes in NSCs (Fig. 2D). Metabolic reporter analysis showed that metabolites such as ATP[c], ADP[c], and phosphoprotein[c] were significantly downregulated in POLG patient iPSCs compared to controls (Fig. 2E). When comparing patient and control NSCs, we found downregulation of metabolic proteins in patient NSCs, including H2O[c], H+[c], H2O[c], NAD+[m], NADH[m], FAD+[m], and FADH2 [m] (Fig. 2F).

We next explored differences in gene expression profile in iPSCs and NSCs carrying $POLG^{homo}$ and $POLG^{comp}$ mutations. We performed principal component analysis (PCA) for $POLG^{homo}$, $POLG^{comp}$ and control lines and found that $POLG^{homo}$, $POLG^{comp}$ and control iPSCs had similar gene expression profiles (Fig. 2G). In NSCs, there was greater heterogeneity among the three groups (Fig. 2G). More notably, more genes were dysregulated between $POLG^{comp}$ NSCs and controls than between $POLG^{homo}$ NSCs and controls (Fig. 2G).

These data suggest that the metabolic dysregulation induced by *POLG* mutations only manifests as cells mature toward neuronal lineage.

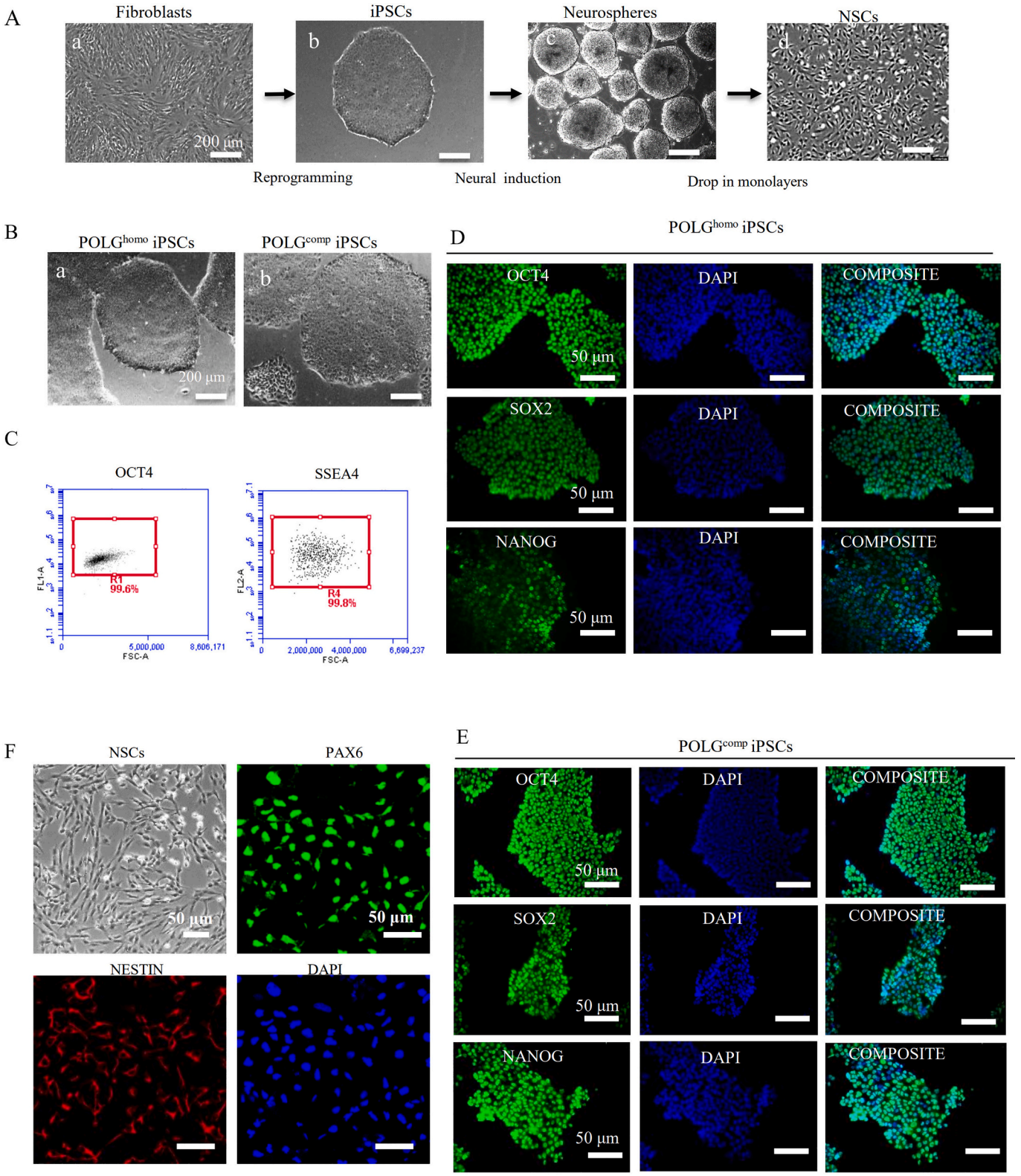

Fig. 1. Generation and characterization of iPSCs and NSCs from POLG^{homo} or POLG^{comp} patient. (A). Flow chart of cell reprogramming and differentiation. The fibroblasts (a) were isolated from two POLG patients carrying either POLG^{homo} or POLG^{comp} and reprogrammed into human iPSCs (b). The iPSCs was further differentiated into NSCs (d) via induction of neurospheres (c). (B). Morphology on phase contrast microscopy for iPSC of POLG^{homo} patient (a) and iPSC of POLG^{comp} patient (b). Scale bars is 200 μm. (C). Flow cytometric quantification of expression level of pluripotent marker OCT4 and SSEA4 in reprogrammed iPSCs. (D, E). Immunofluorescence staining of stem cell markers OCT4, SOX2 and NANOG in POLG^{homo} iPSCs (D) and POLG^{comp} iPSCs (E)). Scale bar is 50 μm. Nuclei are stained with DAPI (blue). (F). Bright field image and immunofluorescence staining of the neural stem cell marker PAX6 and NETSIN in iPSC derived NSCs. Scale bar is 50 μm. Nuclei are stained with DAPI (blue). (For interpretation of the references to colour in this figure legend, the reader is referred to the web version of this article.)

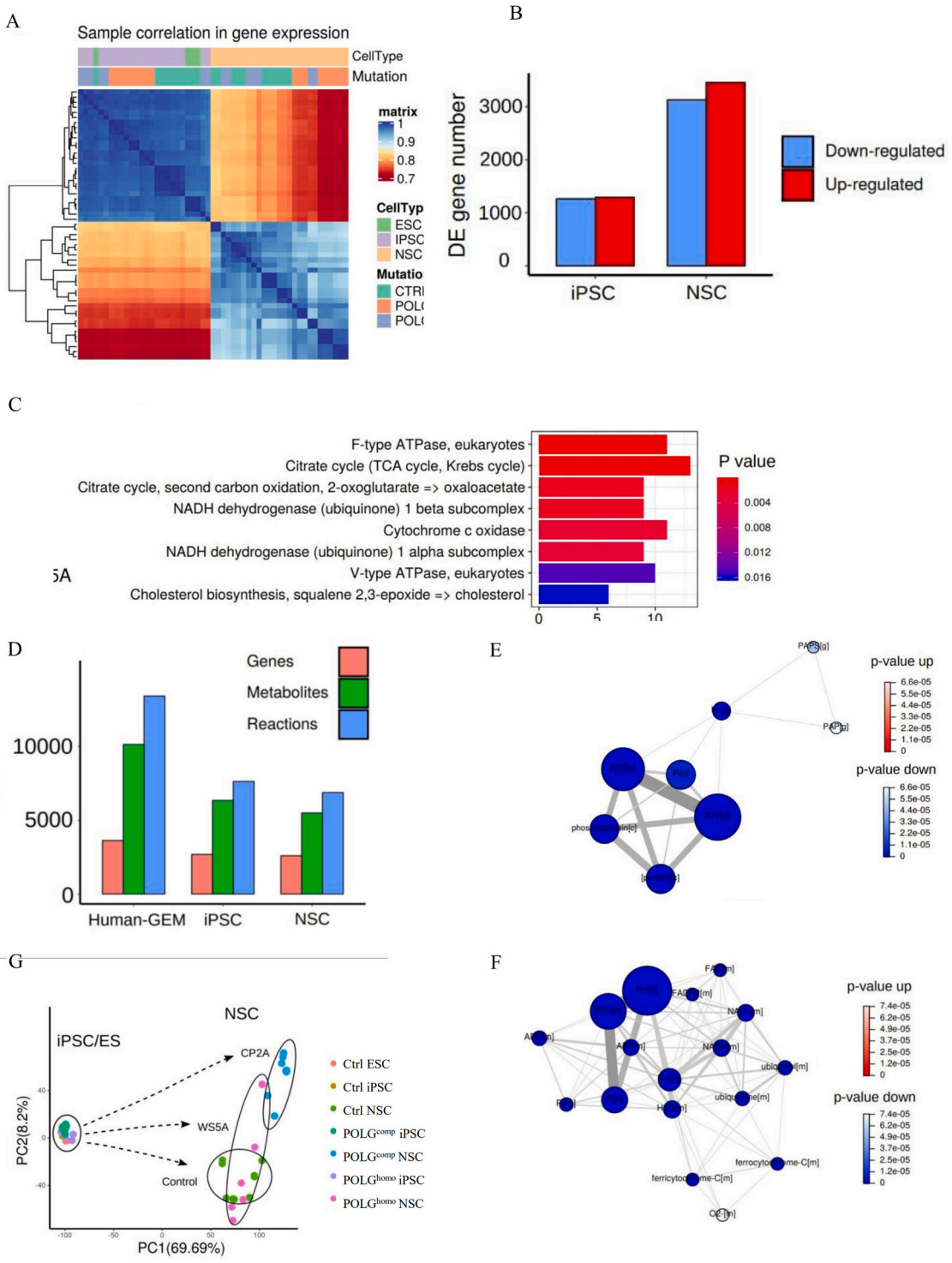

Fig. 2. Transcriptomic status and dysregulated metabolic pathways of POLG patients derived iPSCs and NSCs compared to control. (A). Sample correlation in transcriptomic status of POLG patients derived iPSCs and NSCs, and the corresponding controls. (B). Numbers of up- and downregulated DE genes between POLG patients derived iPSCs and NSCs compared to controls, respectively. (C). Significantly enriched KEGG module pathways of downregulated genes in POLG patients derived NSCs compared with controls. (D). Genome scale metabolic models (GEMs) of iPSCs and NSCs, which were constructed based on transcriptomic data of control iPSC/ES and NSCs using a public human genome-scale metabolic model (Human-GEM) as a reference. (E, F). Metabolic reporter analysis of POLG patients derived iPSCs and NSCs based on iPSC and NSC GEMs, respectively. (G). Principal components analysis of transcriptomic matrix for $POLG^{homo}$ and $POLG^{comp}$ patients derived iPSC and NSCs and controls.

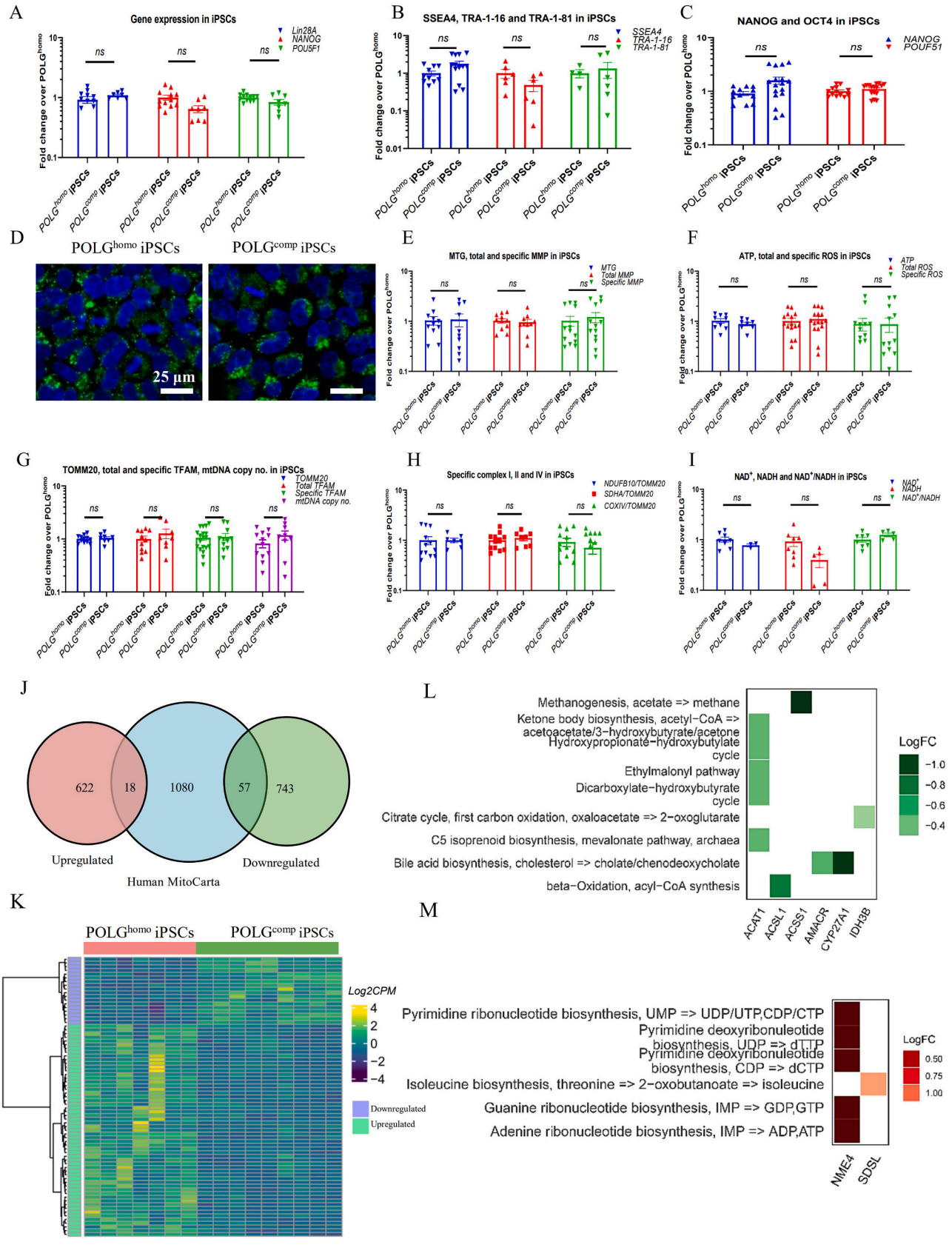

(caption on next page)

Fig. 3. Measurement of mitochondrial function, mtDNA alteration and NAD^+ metabolism in $POLG^{homo}$ and $POLG^{comp}$ iPSCs. (A). QPCR quantification of gene expression for *LIN28A*, *NANOG*, and *POU5F1* for $POLG^{homo}$ and $POLG^{comp}$ patients iPSCs. The fold change is calculated by normalizing all the values to the mean value of $POLG^{homo}$ iPSCs. (B, C). Flow cytometric analysis for pluripotent surface markers SSEA4, TRA-1-60, andTRA-1-81(B), as well as transcription factors NANOG and OCT4 (C) in $POLG^{comp}$ iPSCs compared with $POLG^{homo}$ iPSCs. The fold change is calculated by normalizing all the values to the mean value of $POLG^{comp}$ iPSCs. (D). Confocal images of mitochondrial morphology for $POLG^{homo}$ and $POLG^{comp}$ iPSC lines with MTG staining. Scale bars is 25 μm. Nuclei are stained with DAPI (blue). (E). Flow cytometric analysis of iPSCs for mitochondrial volume (MTG), total MMP (TMRE) and specific MMP (TMRE/MTG) levels. The fold change is calculated by normalizing all the values to the mean value of $POLG^{homo}$ iPSCs. (F). Measurement of intracellular ATP production from luminescent assay and flow cytometric analysis for total intracellular ROS level (DCFDA), and the specific ROS level (DCFDA/MTDR) for $POLG^{homo}$ and $POLG^{comp}$ iPSCs. The fold change is calculated by normalizing all the values to the mean value of $POLG^{homo}$ iPSCs. (G). Flow cytometric analysis for TOMM20, total TFAM and specific TFAM (total TFAM/TOMM20) levels, and relative mtDNA copy number analyzed by QPCR for $POLG^{homo}$ and $POLG^{comp}$ iPSCs. The fold change is calculated by normalizing all the values to the mean value of $POLG^{homo}$ iPSCs. (H). Flow cytometric measurements of mitochondrial complex I, II and IV protein expression at total ad specific level (total complex I, II, IV level/TOMM20). The fold change is calculated by normalizing all the values to the mean value of $POLG^{homo}$ iPSCs. (I). LC-MS-based metabolomics for quantitative measurement of total NAD^+, total NADH level and NAD^+/NADH ratio in $POLG^{homo}$ and $POLG^{comp}$ iPSCs. The fold change is calculated by normalizing all the values to the mean value of $POLG^{homo}$ iPSCs. (J). DE analysis between $POLG^{homo}$ and $POLG^{comp}$ iPSCs using the human MitoCarta 2.0 database as a reference of mitochondrial function related genes. (K). Heatmap of DE expressed mitochondrial function related genes in $POLG^{homo}$ and $POLG^{comp}$ iPSCs. (L-M). KEGG metabolic pathway module classification of down- (L) and upregulated (M) mitochondrial functional related DE genes $POLG^{homo}$ and $POLG^{comp}$ iPSCs. Y-axis represents pathway modules and X-axis represents mitochondrial related DE genes belong to each module. However, none of these pathway modules were significantly enriched. (For interpretation of the references to colour in this figure legend, the reader is referred to the web version of this article.)

2.3. Compound heterozygous and homozygous iPSCs show similar mitochondrial function and transcriptomic profiling

To investigate pluripotency, we next measured pluripotent stem cell-associated gene and marker protein expression. QPCR analysis showed similar expressions of *LIN28A*, *POU5F1* and *NANOG* in $POLG^{homo}$ and $POLG^{comp}$ iPSCs (Fig. 3A). Flow cytometry also detected similar expression levels of all pluripotency markers in both mutant iPSCs, including the pluripotent surface markers SSEA4, TRA-1-60 and TRA-1-81 (Fig. 3B) and the transcription factors OCT4, NANOG (Fig. 3C).

Using MitoTracker Green (MTG) staining and fluorescence confocal microscopy, we determined $POLG^{homo}$ and $POLG^{comp}$ iPSCs had similar morphology (Fig. 3D). Next, we used our previously established flow cytometry method (Liang et al., 2021b) to measure mitochondrial function. We quantified the levels of MTG and tetramethylrhodamine ethyl ester (TMRE) to measure mitochondrial mass and MMP and found that mitochondrial mass measured by MTG, total MMP measured by TMRE, and specific MMP calculated by TMRE/MTG were similar in $POLG^{homo}$ and $POLG^{comp}$ iPSCs (Fig. 3E). ATP production per cell was also similar (Fig. 3F), as was ROS production measured using staining with 2′, 7′- dichlorodihydrofluorescein diacetate (DCFDA) (Fig. 3F). To ensure that this reflected the mitochondrial mass in each cell type, we divided total ROS by a measure of MitoTracker Deep Red (MTDR) to give specific ROS and again found no difference between two mutant iPSCs (Fig. 3F).

We then investigated mitochondrial respiratory chain complex expression in these two mutant iPSCs. We used the complex I subunit NDUFB10 antibody and co-stained with TOMM20 to correlate with mitochondrial mass and found similar levels of complex I in two mutant iPSCs (Fig. 3H). Expression levels of complex II subunit SDHA and complex IV subunit COXIV were also similar in both mutant iPSCs (Fig. 3H). Lastly, we examined the redox state by measuring NAD^+, NADH levels and NAD^+/NADH ratio using liquid chromatography mass spectrometry (LC-MS) and again, found no difference between two mutant iPSCs (Fig. 3I).

Next, we assessed mtDNA copy numbers using flow cytometric analysis of TFAM and qPCR (Liang et al., 2020c). Flow cytometry measurements of TFAM and TOMM20 showed no differences in TOMM20, total TFAM levels, and specific TFAM levels (TFAM/TOMM20) in two mutant iPSCs (Fig. 3G). QPCR measurement of the ND1/APP ratio also revealed similar mtDNA copy number in two mutant iPSCs (Fig. 3G).

To further explore differences in gene expression, we performed RNA sequencing analysis and compared the expression profiles of $POLG^{homo}$ and $POLG^{comp}$ iPSCs. Although PCA showed similarities in both mutant iPSCs (Fig. 1G), we identified 1440 DE genes in $POLG^{comp}$ compared to $POLG^{homo}$ iPSCs: 640 genes were upregulated, and 800 genes were downregulated (Fig. 3J). Applying these data to the human MitoCarta 2.0 database (Calvo et al., 2016) identified 75 DE genes with purported mitochondrial function, of which 18 were upregulated and 57 were downregulated (Fig. 3J, K, Table S2-S3). Subsequent KEGG module analysis showed that the *ACAT1* gene involved in ketone body synthesis and the *IDH3B* gene encoding isocitrate dehydrogenase isoenzyme were significantly downregulated (Fig. 3L), while the *SDSL* and *NME4* genes involved in isoleucine and ribonucleotide biosynthesis were significantly upregulated (Fig. 3M). Despite some changes in modular pathways, metabolic pathway analysis showed no enrichment when comparing $POLG^{comp}$ iPSCs to $POLG^{homo}$ iPSCs.

These data suggest that compound heterozygous and homozygous POLG iPSCs have similar mitochondrial function and metabolic pathway profiles.

2.4. Mitochondrial function impairment is greater in compound heterozygous NSCs than homozygous NSCs

To check the purity of the iPSC derived NSCs, we used flow cytometry and double staining with the neural progenitor markers PAX6 and NESTIN. We showed that 99.9% of cells were positive for both PAX6 and NESTIN (Fig. 4A). Quantification of protein expression revealed significantly elevated levels of PAX6, but lower levels of NESTIN in $POLG^{comp}$ NSCs compared to $POLG^{homo}$ NSCs (Fig. 4B). We assessed mitochondrial structure by transmission electron microscopy and found that both mutant NSCs had similar mitochondrial appearance (Fig. 4C). Using the TMRE/MTG double staining method described above, we found that mitochondrial mass (MTG), total MMPs (total TMRE) were similar in these two mutant NSCs, but the specific MMP levels, i.e., MMPs per mitochondrial mass (total TMRE/MTG) was lower in $POLG^{comp}$ NSCs compared to $POLG^{homo}$ NSCs (Fig. 4D). Direct measurement of intracellular ATP production showed significantly reduced levels in $POLG^{comp}$ NSCs (Fig. 4E). The total and specific levels of intercellular ROS and the total mitochondrial ROS level appeared to be similar, however, $POLG^{comp}$ NSCs had lower specific mitochondrial ROS level compared to $POLG^{homo}$ NSCs (Fig. 4E).

Flow cytometric analysis of TFAM and TOMM20 as described above showed similar expression of TOMM20 and total TFAM, but reduced levels of specific TFAM, indicating a lower amount of mtDNA, which was confirmed by qPCR that showed lower ND1/APP ratio in $POLG^{comp}$ NSCs (Fig. 4F). Flow cytometry analysis revealed a greater loss of specific complex I levels in $POLG^{comp}$ NSCs than $POLG^{homo}$ NSCs, while specific levels of complex II and IV were the same (Fig. 4G). Furthermore, LC-MS measurement showed that NAD^+ level and NADH level were lower in $POLG^{comp}$ NSCs compared to $POLG^{homo}$ NSCs, while the

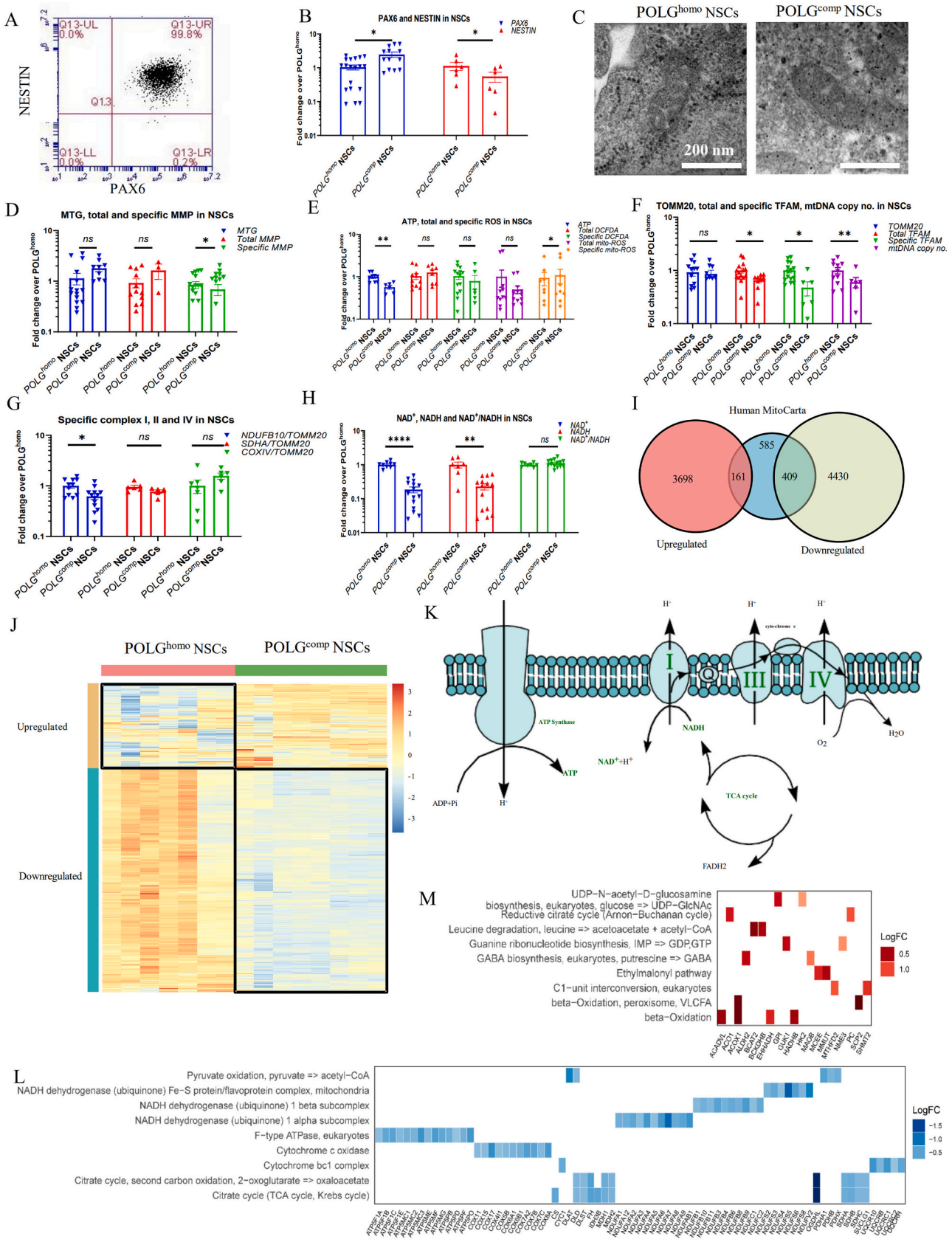

(caption on next page)

Fig. 4. Measurement of mitochondrial function, mtDNA alteration and NAD^+ metabolism in $POLG^{homo}$ and $POLG^{comp}$ NSCs. (A). Flow cytometric analysis for double staining of the NESTIN and PAX6 in iPSC derived NSCs. (B). Flow cytometric analysis for the expression of NESTIN and PAX6 in $POLG^{comp}$ NSCs compared with $POLG^{homo}$ NSCs. The fold change is calculated by normalizing all the values to the mean value of $POLG^{comp}$ NSCs. (C). Representative transmission electron microscopy images of mitochondrial structures in $POLG^{homo}$ and $POLG^{comp}$ NSCs. Scale bar is 200 nm. (D). Flow cytometric analysis of iPSCs for mitochondrial mass (MTG), total MMP (TMRE) and specific MMP (TMRE/MTG) levels. The fold change is calculated by normalizing all the values to the mean value of $POLG^{comp}$ NSCs. (E). Measurement of intracellular ATP production from luminescent assay and flow cytometric analysis for total intracellular ROS level (DCFDA), and the specific ROS level (DCFDA/MTDR) for $POLG^{homo}$ and $POLG^{comp}$ NSCs. The fold change is calculated by normalizing all the values to the mean value of $POLG^{comp}$ NSCs. (F). Flow cytometric analysis for TOMM20, total TFAM and specific TFAM (total TFAM/TOMM20), and relative mtDNA copy number analyzed by qPCR for $POLG^{homo}$ and $POLG^{comp}$ NSCs. The fold change is calculated by normalizing all the values to the mean value of $POLG^{comp}$ NSCs. (G). Flow cytometric measurements of mitochondrial complex I, II and IV protein expression at specific level (total complex I, II, IV level/TOMM20) in $POLG^{homo}$ and $POLG^{comp}$ NSCs. The fold change is calculated by normalizing all the values to the mean value of $POLG^{comp}$ NSCs. (H). LC-MS-based metabolomics for quantitative measurement of total NAD^+, total NADH level and NAD^+/NADH ratio in $POLG^{homo}$ and $POLG^{comp}$ NSCs. The fold change is calculated by normalizing all the values to the mean value of $POLG^{homo}$ NSCs. (I). DE analysis between $POLG^{homo}$ and $POLG^{comp}$ NSCs using the human MitoCarta 2.0 database as a reference of mitochondrial function related genes. (J). Heatmap of DE expressed mitochondrial function related genes in NSCs between $POLG^{homo}$ and $POLG^{comp}$ lines. (K). Illustration of downregulated mitochondrial functional related pathway modules and metabolites in $POLG^{comp}$ compared with $POLG^{homo}$ NSCs. Involved pathways and metabolites are in green. (L). KEGG metabolic pathway module classification of downregulated DE expressed mitochondrial functional genes in $POLG^{comp}$ compared with $POLG^{homo}$ NSCs. (M). KEGG metabolic pathway module classification of upregulated DE expressed mitochondrial functional genes in $POLG^{comp}$ NSCs compared with $POLG^{homo}$ NSCs. Y-axis represents pathway modules and X-axis represents mitochondrial related DE genes belong to each module. (For interpretation of the references to colour in this figure legend, the reader is referred to the web version of this article.)

ratio of NAD^+/NADH levels remained unchanged (Fig. 4H).

These data suggest that the presence of compound heterozygous *POLG* mutations in NSCs results in greater mitochondrial functional dysfunction than occurs with homozygous mutations.

2.5. Compound heterozygous NSCs showed greater transcriptome defects than homozygous NSCs

Next, we asked whether different NSC genotypes displayed distinct transcriptomic signatures. PCA analysis revealed a clear difference in PCA profiles between $POLG^{comp}$ and $POLG^{homo}$ NSCs (Fig. 2G). For comparison, we used 6 $POLG^{comp}$ samples with 2 individual clones each and 3 replicates each, and 9 $POLG^{homo}$ samples with 3 individual clones, 3 replicates each. Compared to $POLG^{homo}$ NSCs, there were 8698 DE genes in $POLG^{comp}$ NSCs, of which 4839 were downregulated and 3859 were up-regulated (Fig. 4I). Enrichment for mitochondrial function-related genes detected 161 upregulated and 409 downregulated genes (Fig. 4I, Tables S4-S5). This predominance of downregulated DE genes (Fig. 4J) in $POLG^{comp}$ NSCs comprised genes in key mitochondrial functional modules involved in electron transport and energy production processes (Fig. 4K, Tables S4-S5). Notably, key regulatory genes involved in pyruvate oxidation (pyruvate $\geq$ acetyl-CoA), including genes encoding different components of the pyruvate dehydrogenase complex, such as *E1 (PDHA1, PDHB)*, *E2 (DLAT)*, *E3 (DLD)* and *PDHX* (Fig. 4L). Other downregulated genes included genes involved in encoding oxoglutarate dehydrogenase complex (*OGDHL*, *DLD*, *DLST*), succinate-CoA ligase genes (*SUCLG1*), succinate dehydrogenases (SDHA, SDHB, SDHC), fumarate (FH) and malate dehydrogenases (*MDH1*, *MDH2*) (Fig. 4L).

Consistent with our functional investigations, we found down-regulation of the genes encoding respiratory chain complex I proteins including *NDUFA1-A8*, β-subcomplex-related genes *NDUFB1, NDUFB3-B4, NDUFB6, NDUFB8-B11, NDUFC1* and the mitochondrial Fe-—S protein-related genes *NDUFS2-S6*, *NDUFS8*, and *NDUFV2* (Fig. 4L). Multiple genes encoding respiratory chain complex V proteins including catalytic core-related proteins (including *ATP5F1A*, *ATP5F1B*, *ATP5F1C*, *and ATP5F1E*) and proton channel subunit-related proteins (including *ATP5PB*, *ATP5PD*, *ATP5PF*, *ATP5PO*) and those involved in *F1/Fo ATPase* fundtion (including *ATP5MC1-C3, ATP5ME*, *ATP5MF and ATP5MG*) (Fig. 4L) were also downregulated. Genes encoding complex III proteins (cytochrome *bc*1*: CYC1*, *UQCRB*, *UQCRC1* and *UQCRC2*, *UQCR10*, *UQCRH,* etc.) and complex IV proteins (cytochrome *c* oxidase: *COX6B1*, *COX7A2*, *COX8A,* etc.) were also downregulated (Fig. 4L). Pathway enrichment analysis of KEGG modules revealed that down-regulated genes in $POLG^{comp}$ NSCs were mainly distributed in β-oxidation (including *ACADVL*, *ACOX1*, *EHHADH*, *HADHB*), proline biosynthesis (including *ALDH18A1* and *PYCR1*) and isoleucine biosynthesis (including *BCAT2* and *SDSL*) (Fig. 4L). Although upregulated genes were present in $POLG^{comp}$ NSCs relative to $POLG^{homo}$ NSCs, these genes were not significantly different (Fig. 4M)

These findings suggest that compound heterozygous *POLG* mutations lead to more severe dysregulation of metabolic pathways in NSCs.

2.6. Greater mitochondrial defects in compound heterozygous NSCs led to cellular senescence and mitophagy activation

Since our findings suggested greater mitochondrial dysfunction in compound heterozygous NSCs, we asked what the cellular consequences of these changes were. Given changes in NAD^+ metabolism and complex I and the known link between mitochondrial dysfunction and increased ROS production and senescence, we investigated cellular senescence and mitophagy in NSCs. To examine cellular senescence, we performed β-galactosidase staining and flow cytometry to measure the cellular senescence marker p16INK4. We observed a significant increase in β-galactosidase activity in $POLG^{comp}$ versus $POLG^{homo}$ NSCs (Fig. 5A, B). This finding was further confirmed by p16INK4 expression measured by flow cytometry (Fig. 5B).

Next, we investigated the molecular pathways that initiate cellular senescence. Sirtuin 1 (SIRT1) is an NAD^+-dependent deacetylase that plays a key role in many cellular processes including energy metabolism, stress response and aging (Marcus and Andrabi, 2018). SIRT1 also regulates the expression of the mitochondrial uncoupling protein 2 (*UCP2*) gene and overexpression of which can reduce MMPs and induce senescence (Marcus and Andrabi, 2018). We investigated the expression of phosphorylated SIRT1 (Ser47) (p-SIRT1) and UCP2 using western blotting and found that p-SIRT1 (Ser47) was reduced in $POLG^{comp}$ NSCs compared to $POLG^{homo}$ NSCs, although UCP2 expression remained unchanged (Fig. 5C, D).

Mitophagy is required for both promotion and inhibition of senescence and senescence-related phenotypes (Moiseeva et al., 2009). To investigate whether mitophagy was altered, we investigated the mitophagy-related proteins LC3B, BNIP3, PINK1 and Parkin using western blotting. This revealed elevated level of LC3B-II and elevated LCBII/LC3BI ratio in $POLG^{comp}$ NSCs, indicating autophagy activation (Fig. 5C, E). Accumulation of BNIP3 was also observed in $POLG^{comp}$ NSCs, but not in $POLG^{homo}$ cells (Fig. 5C, E). The expression of PINK1 and Parkin was similar in both mutant NSCs (Fig. 5C, E).

These findings suggest that the more severe mitochondrial damage in heterozygous POLG variants results in increased cellular senescence through downregulation of p-SIRT1 and activation of mitophagy regulated by BNIP3.

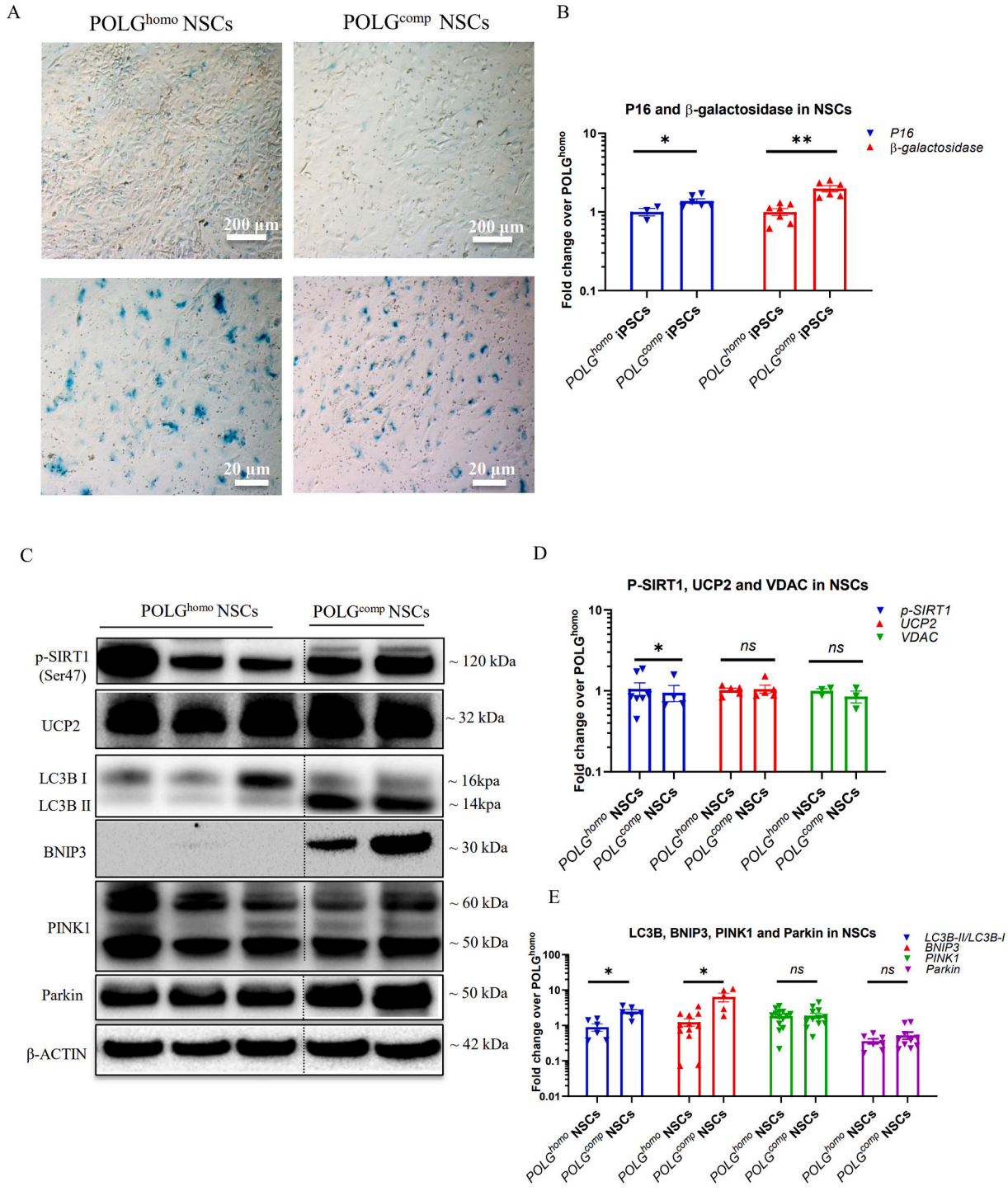

Fig. 5. POLG^{comp} NSCs exhibited senescence phenotype and mitophagy activation compared to POLG^{homo} NSCs. (A, B). Representative images of senescence β-galactosidase staining (A) and quantification (B) by calculating the percentage of positively stained cells by division of the negative cells from A in POLG^{comp} NSCs compared to POLG^{homo} NSCs. Scale bars is 20 μm or 200 μm. The fold change in B is calculated by normalizing all the values to the mean value of POLG^{homo} NSCs. (C-E). Representative images (C) and quantification (D, E) for western blotting with p-SirT1 (Ser47), UCP2, VDAC, LC3B, BNIP3, PINK1, Parkin and β-ACTIN. Three independent experiments are included. The fold change in D and E is calculated by normalizing all the values to the mean value of POLG^{homo} NSCs.

2.7. The effect on mitochondrial function is similar in compound heterozygous and homozygous astrocytes

Next, we tested the effect of different genotypes in astrocytes. We differentiated astrocytes from NSCs using a previously described protocol (Liang et al., 2020a). Cell morphology was similar in both mutant astrocytes (Fig. 6A) and confocal images showed positive staining for astrocyte lineage markers GFAP and S100β, and astrocyte functional markers EAAT1 and glutamine synthesis (GS) (Fig. 6A). Differentiated astrocytes also stained negative for the neural marker doublecortin (DCX) (Fig. S3), indicating no contamination of neural lineage. Flow cytometric analysis confirmed that astrocytes were over 98% positive for astrocyte marker GFAP and CD44, and functional marker EAAT1 and GS (Fig. 6B). Quantification of the protein levels of these astrocyte

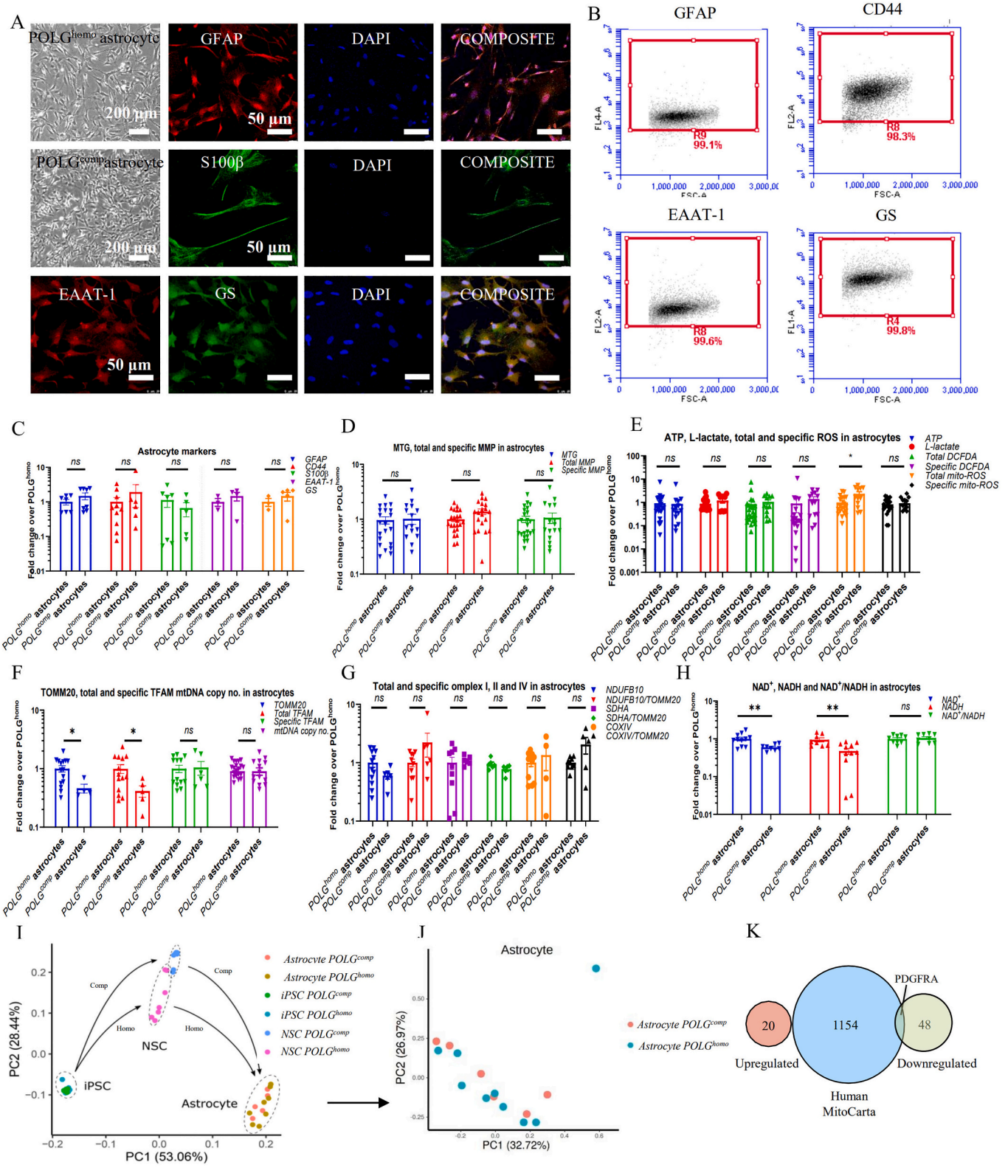

(caption on next page)

Fig. 6. Measurement of mitochondrial function, mtDNA alteration and NAD^+ metabolism in $POLG^{homo}$ and $POLG^{comp}$ astrocytes. (A). Representative phase-contrast images of the iPSC-derived astrocytes generated from in $POLG^{comp}$ and $POLG^{homo}$ astrocytes and confocal images of astrocyte lineage markers GFAP and S100β, and functional markers EAAT-1 and GS. Scale bar is 200 μm or 50 μm. Nuclei are stained with DAPI (blue). (B). Flow cytometric analysis for GFAP, CD44, EAAT-1 and GS in astrocytes. (C). Flow cytometric analysis for the expression of GFAP, CD44, S100β, EAAT-1 and GS in $POLG^{comp}$ astrocytes compared with $POLG^{homo}$ astrocytes. The fold change is calculated by normalizing all the values to the mean value of $POLG^{homo}$ astrocytes. (D). Flow cytometric analysis for mitochondrial volume (MTG), total MMP (TMRE) and specific MMP (TMRE/MTG) levels in $POLG^{comp}$ astrocytes compared with $POLG^{homo}$ astrocytes. The fold change is calculated by normalizing all the values to the mean value of $POLG^{homo}$ astrocytes. (E). Measurement of intracellular ATP production from luminescent assay and flow cytometric analysis for total intracellular ROS level (DCFDA), and the specific ROS level (DCFDA/MTDR) for $POLG^{homo}$ and $POLG^{comp}$ astrocytes. The fold change is calculated by normalizing all the values to the mean value of $POLG^{homo}$ astrocytes. (F). Flow cytometric analysis for TOMM20, total TFAM and specific TFAM (total TFAM/TOMM20), and relative mtDNA copy number analyzed by qPCR for $POLG^{homo}$ and $POLG^{comp}$ astrocytes. The fold change is calculated by normalizing all the values to the mean value of $POLG^{homo}$ astrocytes. (G). Flow cytometric measurements of mitochondrial complex I, II and IV protein expression at total and specific level (total complex I, II, IV level/TOMM20) in $POLG^{homo}$ and $POLG^{comp}$ astrocytes. The fold change is calculated by normalizing all the values to the mean value of $POLG^{homo}$ astrocytes. (H). LC-MS-based metabolomics for quantitative measurement of total NAD^+, total NADH level and NAD^+/NADH ratio in $POLG^{homo}$ and $POLG^{comp}$ astrocytes. The fold change is calculated by normalizing all the values to the mean value of $POLG^{homo}$ astrocytes. (I). PCA analysis of $POLG^{comp}$ and $POLG^{homo}$ iPSCs, NSCs and astrocytes. (J). PCA analysis of $POLG^{comp}$ and $POLG^{homo}$ astrocytes. (K). DE analysis between $POLG^{homo}$ and $POLG^{comp}$ astrocytes using the human MitoCarta 2.0 database as a reference of mitochondrial function related genes. (For interpretation of the references to colour in this figure legend, the reader is referred to the web version of this article.)

markers showed similar levels of GFAP, CD44, S100β, EAAT1, and GS in two mutant astrocytes (Fig. 6C).

Using the same experimental approach as described above, we found that $POLG^{comp}$ and $POLG^{homo}$ astrocytes exhibited similar mitochondrial mass (MTG) and total (total TMRE) and specific levels of MMP (TMRE/MTG) (Fig. 6D). Although lower level of total mitochondrial ROS was detected in $POLG^{comp}$ versus $POLG^{homo}$ astrocytes, no difference in levels of ATP production, lactate production, total and specific intracellular ROS, specific mitochondrial ROS were detected between the two mutant astrocytes (Fig. 6E). We found lower expression of TOMM20 and total TFAM in $POLG^{comp}$ astrocytes (Fig. 6F), but there was no change in specific TFAM level (TFAM/TOMM20), and qPCR measurement showed no difference in mtDNA copy number between the two mutant astrocytes (Fig. 6F). Measurements of the complexes I, II,IV at both total and specific levels showed no difference between the two mutant astrocytes (Fig. 6G). Measurements of NAD biosynthesis showed significantly reduced levels of NAD^+ and NADH in $POLG^{comp}$ astrocytes versus $POLG^{homo}$ astrocytes, but the ratio of NAD^+/NADH was similar (Fig. 6H).

We then investigated the transcriptional signature of $POLG^{comp}$ and $POLG^{homo}$ astrocytes. We found in PCA analysis that although NSCs from both genotypes showed greater heterogeneity, astrocytes differentiated from the two groups of NSCs did not differ significantly in RNA expression (Fig. 7I, J). In a DE analysis comparing $POLG^{comp}$ and $POLG^{homo}$ astrocytes, we found only 69 genes whose expression was significantly changed, including 20 upregulated genes and 49 downregulated genes (Fig. 7K). Notably, only one gene, *PDGFRA*, belonging to the MitoCarta mitochondrial gene database, was downregulated in $POLG^{comp}$ astrocytes than in $POLG^{homo}$ astrocytes (Fig. 7K).

These studies demonstrate that the genotype-defined mitochondrial and transcriptional differences seen in NSCs are lost in the astrocyte lineage, even though astrocytes are derived from NSCs.

2.8. Compound heterozygous POLG NSCs have a lower potential for differentiation to DA neurons than homozygous NSCs

Our previous clinical study showed that DA neurons in the substantia nigra are among the most severely affected cell types in POLG patients (Tzoulis et al., 2014b). We also reported previously that NSC-derived DA neurons exhibit defective mitochondrial function and mtDNA depletion with a trend suggesting a greater defect in $POLG^{comp}$ than in $POLG^{homo}$ neurons (Liang et al., 2021a). In this current study, we asked whether differences in mitochondrial damage between compound heterozygous and homozygous NSCs affected the differentiation efficiency toward the commitment of DA neurons. To do this, we used 3 separate $POLG^{homo}$ NSCs clones and 4 separate $POLG^{comp}$ NSCs clones and performed DA differentiation multiple times. $POLG^{comp}$ NSCs were consistently less efficient at differentiating neurons than $POLG^{homo}$ cells (Fig. 7A): all $POLG^{homo}$ NSCs were fully capable of generating DA neurons, whereas only 3/14 $POLG^{comp}$ iPSCs clones generated DA neurons (Fig. 7A).

We tested this further in a three-dimensional (3D) system using the hanging drop technique to make 3D spheroids and iPSC-derived neuronal progenitors, astrocytes, and oligodendrocytes, as previously described (Liang et al., 2020a). We found that both POLG spheroids were smaller than control lines, but $POLG^{comp}$ spheroids were even smaller in size and had less expression of the neural marker DCX compared to $POLG^{homo}$ spheroids (Fig. 7B).

These data suggest that the more severe mitochondrial dysfunction found in compound heterozygous POLG variants results in a reduced neural differentiation potential compared to homozygous variants.

2.9. Compound heterozygous POLG fibroblasts had similar mitochondrial function compared to homozygous POLG fibroblasts

We demonstrated above that mitochondrial function were more damaged in compound heterozygous neurons, and then we wondered whether this difference was manifested in parental fibroblasts. We then performed the same functional studies to examine mitochondrial-related features. When comparing $POLG^{comp}$ fibroblasts with $POLG^{homo}$ fibroblasts, we observed similar cell morphology observed and mitochondrial morphology observed by MTG staining under confocal microscopy (Fig. 7C). Flow cytometry analysis showed similar mitochondrial mass (MTG), total MMP levels measured by TMRE and specific MMP level quantified by the ratio of total TMRE to MTG in the two patient fibroblasts (Fig. 7D). ATP production measurements showed that ATP level, total and specific ROS levels in $POLG^{comp}$ and $POLG^{homo}$ fibroblasts were similar (Fig. 7E).

We then compared changes in mtDNA copy number in fibroblasts from these two patients using the same methods described above. Flow cytometry analysis showed that both patients had similar total and specific levels of TFAM (Fig. 7F), as well as for TOMM20 level, indicating the same mitochondrial mass (Fig. 7F). QPCR also revealed similar mtDNA copy number in both mutant fibroblasts (Fig. 7F). We then determined the protein levels of mitochondrial complexes and found no significant differences in total and specific levels of complexes I, III and IV between the two patient fibroblasts (Fig. 7G).

These results suggest that compound heterozygous and homozygous POLG variants display similar mitochondrial function in fibroblasts.

3. Discussion

Mutations in *POLG* give syndromes with variable clinical features and interestingly, different degrees of severity. While much has been learned about the cellular consequences of *POLG* mutations, establishing genotype-phenotype correlations have remained elusive. To address this question, we used reprogramming of patient-specific iPSCs to assess

A

Lines	POLG^{homo} clone1	POLG^{homo} clone2	POLG^{homo} clone3	POLG^{comp} clone1	POLG^{comp} clone1	POLG^{comp} clone2	POLG^{comp} clone3
DA neuron differentiation efficiency	5/5	6/6	3/3	2/4	1/4	0/3	0/3

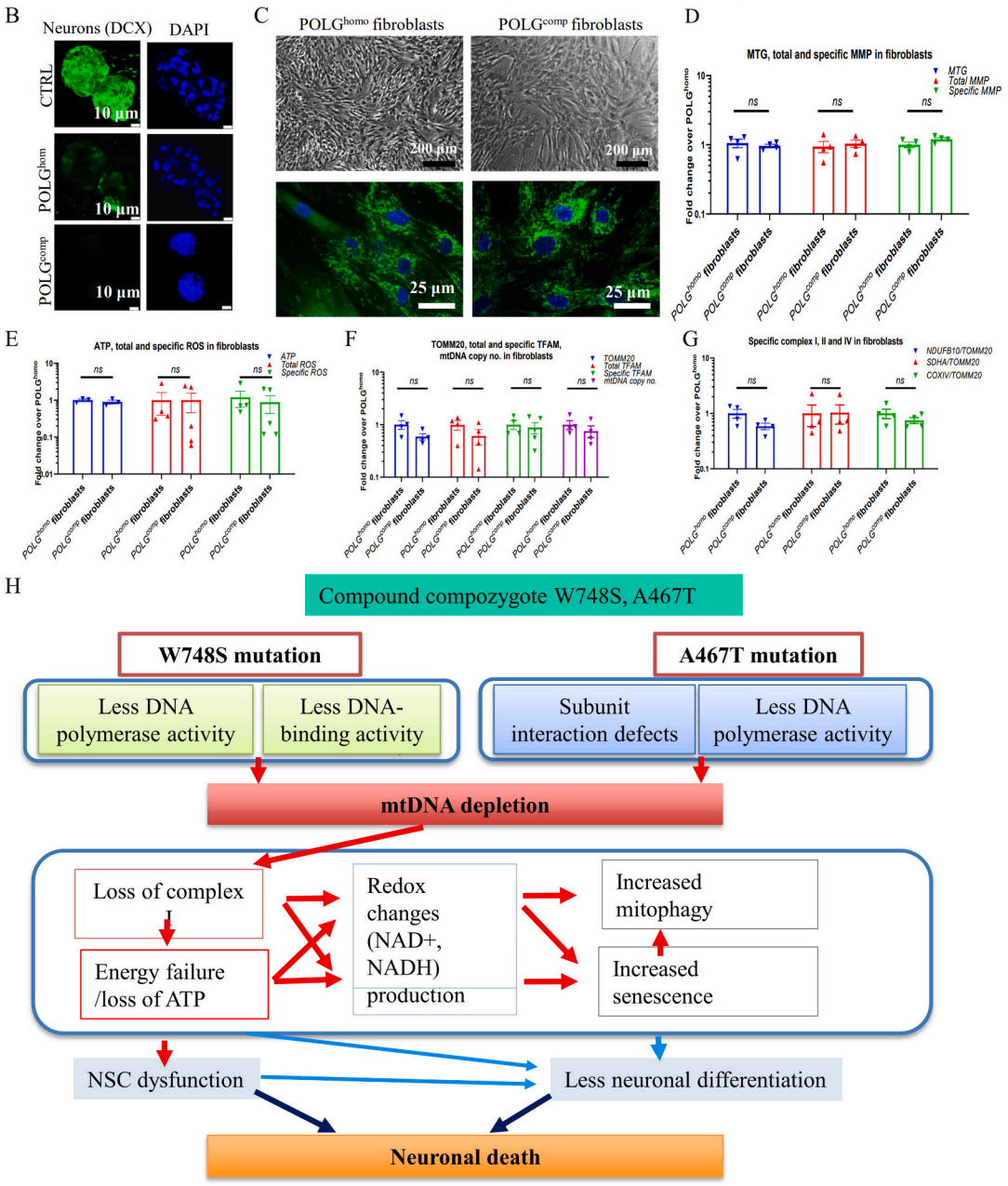

Fig. 7. DA neural differentiation efficiency of POLG^{homo} and POLG^{comp} cells and measurement of mitochondrial function, mtDNA alteration in POLG^{homo} and POLG^{comp} fibroblasts. (A). DA neuron differentiation efficiency in individual clones from POLG^{homo} and POLG^{comp} iPSCs. (B). Representative confocal microscopy images of DCX staining of neurospheres made from NSCs, astrocytes and oligodendrocytes derived from POLG^{homo}, POLG^{comp} and control iPSCs. (C). Representative phase-contrast and confocal microscopy images with MTG staining in POLG^{homo} and POLG^{comp} fibroblasts. Scale bar is 200 µm or 25 µm. Nuclei are stained with DAPI (blue). (D). Flow cytometric analysis for MTG, total MMP (TMRE) and specific MMP (TMRE/MTG) in POLG^{homo} and POLG^{comp} fibroblasts. The fold change is calculated by normalizing all the values to the mean value of POLG^{homo} fibroblasts. (E). Measurement of intracellular ATP production from luminescent assay and flow cytometric analysis for total intracellular ROS level (DCFDA), and the specific ROS level (DCFDA/MTDR) for POLG^{homo} and POLG^{comp} fibroblasts. The fold change is calculated by normalizing all the values to the mean value of POLG^{homo} fibroblasts. (F). Flow cytometric analysis for TOMM20, total TFAM and specific TFAM (total TFAM/TOMM20), and relative mtDNA copy number analyzed by qPCR for POLG^{homo} and POLG^{comp} fibroblasts. The fold change is calculated by normalizing all the values to the mean value of POLG^{homo} fibroblasts. (G). Flow cytometric measurements of mitochondrial complex I, II and IV protein expression at total and specific level (total complex I, II, IV level/TOMM20) in POLG^{homo} and POLG^{comp} fibroblasts. The fold change is calculated by normalizing all the values to the mean value of POLG^{homo} fibroblasts. (H). Summary of the possible disease mechanisms in neuronal death with the patient carrying *POLG* compound heterozygous mutation. (For interpretation of the references to colour in this figure legend, the reader is referred to the web version of this article.)

mutation-specific neuropathology. We generated iPSCs from two patients, one homozygous for c.2243G > C (p.W748S) and the other compound heterozygous for c.2243G > C and c.1399G > A (p.A467T) mutations. Our earlier clinical studies showed that patients exhibit progressive neurological disease regardless of genotype, but major differences in survival could be observed depending on genotype, with compound heterozygotes having significantly shorter survival times than homozygous patients (Tzoulis et al., 2006a). In this present study, we found that compound heterozygous cells do indeed demonstrate a more severe defect in mitochondrial function than homozygous cells, findings supported by transcriptomic analysis showing more severe dysregulation of multiple metabolic pathways, but this only occurred in neural lineage cells, not in the original iPSCs, astrocytes, orfibroblasts.

The *POLG* mutants A467T and W748S affect the catalytic subunit through apparently distinct mechanisms. The W748S is located in the linker region, and it has been suggested that the W748S substitution would destabilize this subdomain and affect DNA polymerase activity (Lee et al., 2009). The W748S mutation causes low DNA polymerase activity, low DNA polymerase processivity, and defective DNA binding (Chan et al., 2006). In contrast, the A467T is located in the terminal thumb region of Pol γ in close contact with the dimeric auxiliary subunit (POLG2). It interacts with the template DNA and the helper subdomain and forms a major surface of the DNA binding channel (Farnum et al., 2014). Functional studies have shown that the A467T mutant has both low polymerase activity and subunit interaction defects (Chan et al., 2005). That different mutations affect mtDNA replication defects in different ways raises the possibility that there are cumulative effects in compound heterozygotes resulting in a more severe phenotype than homozygotes. Furthermore, since different tissues manifest different mtDNA defects in the presence of the same *POLG* mutations, e.g., neurons show mtDNA depletion while skeletal muscle shows multiple deletions, it is necessary to examine the question of genotype: phenotype correlation in specific tissues. Since it was not possible to do this in living patients, we turned to a tractable model system based on stem cell technology.

We have already shown that POLG iPSC derived NSCs replicate the cellular phenotypes found in postmortem neurons (Liang et al., 2020c). In the current study, we show that, at the cellular level, the degree of mtDNA dysfunction in NSCs varies according to mutation: compound heterozygotes show a more pronounced mtDNA depletion and more impaired mitochondrial function, including MMP reduction, ATP production, and mitochondrial complex I level. Since complex I of the respiratory chain re-oxidizes reduced NADH to NAD^+, loss of complex I will have a major impact on metabolism generally. At the transcriptional level, we see this in our transcriptomic findings a clear difference between with compound heterozygotes and homozygous *POLG* mutations, with downregulation of mitochondrial function-related genes in compound heterozygotes, including genes in key mitochondrial functional modules involved in electron transport and energy production processes. Our findings suggest that more impaired mitochondrial function in heterogeneous NSCs may be reflected in core steps of mitochondrial energy production, and that these abnormalities ultimately lead to more severe ATP production defects compared to homozygotes, which further affects the differentiation capacity of these NSCs to generate committed neurons.

Transcriptomics revealed clear differences between compound heterozygous and homozygous POLG NSCs, with downregulation of genes related to mitochondrial function in compound heterozygous NSCs, including genes in key mitochondrial functional modules involved in electron transport and energy production processes. Consistent with our functional studies, we found that genes encoding respiratory chain complex I, III, IV, and V proteins were downregulated, illustrating abnormalities in oxidative phosphorylation metabolism in compound heterozygous NSCs. Glycolysis, along with oxidative respiration, is the primary metabolic pathway employed by cells to transform biochemical energy from nutrients into ATP for cellular function. Pyruvate produced by glycolysis is transported to the mitochondria, where it enters the TCA cycle under and then is converted to lactate. Under hypoxic conditions or pathology, the rate of glycolysis increases to compensate for reduced oxidative respiration to meet cellular energy demands. We found that mitochondrial pyruvate and lactate metabolism-related pathways and genes were also significantly down-regulated in transcriptomics. These findings suggest that more impaired mitochondrial function in compound heterozygous NSCs reflects not only core steps in mitochondrial energy production, especially oxidative phosphorylation, but also abnormalities in the pyruvate and lactate energy metabolism axes that ultimately lead to more severe ATP production deficiency in compound heterozygotes.

Mitochondrial dysfunction plays an important role in multiple feedback loops that induce cellular senescence *in vitro* (Moiseeva et al., 2009) and *in vivo* (Kang et al., 2013). Cellular senescence is a complex stress response by which proliferating cells lose their ability to divide and enter cell cycle arrest. Growing evidence also suggests that senescent cells accumulate with age, a process that may contribute to age-related phenotypes and pathology (Song et al., 2020). Several studies suggest that mitochondrial ROS are involved in this process. ROS can damage nuclear DNA, thereby activating the DNA damage response to induce senescence (Moiseeva et al., 2009). On the other hand, metabolic decline can also lead to oxidative stress and DNA damage. We found that the more severe mitochondrial dysfunction and reduction of MMP in compound heterozygotes could lead to increased production of ROS and failure of NADH reoxidation, suggesting that both may be involved in the senescence response seen in these NSCs. While mitochondrial dysfunction drives and maintains cellular senescence (Moiseeva et al., 2009; Correia-Melo et al., 2016), senescence itself, particularly persistent DNA damage response signaling, also directly contributes to senescence-associated mitochondrial dysfunction (Chapman et al., 2019). It is possible therefore, that both mechanisms are active in in POLG compound heterozygotes NSCs.

In addition to senescence, we found that another cellular consequence induced by the more severe mitochondrial damage in compound heterozygotes involved mitophagy. Mitophagy plays a role in maintaining mitochondrial health. Mitophagy can either specifically eliminate the damaged or dysfunctional mitochondria or clear all mitochondria during specialized developmental stages. The activation of mitophagy is observed in brain damage induced by cerebral ischemia (Lan et al., 2018). Similar, our finding on the upregulation of BNIP3 and LC3B protein levels and occurrence of mitochondrial autophagosomes in NSCs with compound heterozygous *POLG* mutations suggested active degradation through mitophagy. More importantly, given the mitophagy is an essential mitochondrial quality control mechanism implicated in senescence and it can also be induced by mitochondrial stress (Wang et al., 2012). Our finding of the more mitochondrial damage in NSCs for compound heterozygotes than homozygotes may lead to the cell fate of both mitophagy activation and senescence and later will even enhance the mitochondrial stress. Study in stroke revealed that BNIP3 exclusively activates excessive mitophagy leading to cell death (Shi et al., 2014). Therefore, the activation of mitophagy at the NSC stage may lead to a decrease in the efficiency of DA neuron differentiation in POLG compound heterozygous cells.

In the present study, we found that patient fibroblasts and iPSCs in compound heterozygotes appeared to be able to maintain their MMP, mitochondrial mass, and mtDNA replication at similar levels as homozygotes (Fig. S5). They also appear to be able to modulate their redox homeostasis. Interestingly, when NSCs were differentiated into astrocytes, mitochondrial function appeared relatively similar in compound heterozygotes and homozygotes, even though these cells were derived from NSCs with clear differences in the severity of the mitochondrial defect. This is similar to what we see in fibroblasts and suggests that cells such as these, that are highly dependent on glycolysis for energy generation, are in some way protected from the most damaging consequences.

In conclusion, our study shows that it is possible to construct a genotype-phenotype correlation to explain why patients with compound heterozygotes mutations have a poorer prognosis than those with homozygous *POLG* mutations. In compound heterozygotes, mitochondrial function is more impaired than homozygotes and the effects on other metabolic pathways particularly energy metabolism, are more profound. We find also that there is also greater activation of cellular senescence and pathways required for clearing damaged mitochondria (Fig. 7H). That this is restricted to neural lineage cells, and for example not seen in astrocytes, is also important. Our observations from post-mortem studies showed that a major astrocyte response to the neuronal damage and necrosis suggesting that this cell type remains functional. Whether this difference can be explained by two mutations affecting polymerase function in different ways remains unclear. We did, however, find lower mtDNA copy number in heterozygous cells suggesting that this possibility remains.

4. Material and methods

4.1. Ethical permission

The project was approved by the Western Norway Committee for Ethics in Health Research (REK nr. 2016/578). Tissues were acquired with written informed consent from all patients.

4.2. Generation of iPSCs, NSCs, DA neurons and astrocytes

Skin biopsies were collected from POLG patients and fibroblasts were isolated. Ethical approval was granted from Norwegian Research Ethics Committee ((2016/578). Fibroblasts were cultured in medium consisted of DMEM/F12, GlutaMAX™ (Thermo Fisher Scientific, # 35050061), and 10% (*v*/v) Fetal Bovin Serum (FBS, Sigma-Aldrich, # 12103C). Fibroblasts were reprogrammed to iPSCs as previously described (Liang et al., 2020c). IPSCs were grown under feeder-free condition using E8 medium (Invitrogen, # A1517001) on Geltrex-coated 6-well plates. The generation of NSCs and DA neurons were described previously (Liang et al., 2020c). Astrocytes were differentiated from NSCs according to the protocol described previously (Liang et al., 2020a).

4.3. Immunofluorescence staining

Live cells grown on coverslips were fixed with 4% (v/v) paraformaldehyde (PFA) for 10 min. Then the cells were blocked using blocking buffer composed of 1X PBS, 10% (v/v) normal goat serum (Sigma-Aldrich, # G9023) and 0.3% (v/v) Triton X-100 (Sigma-Aldrich, # X100-100ML) for 1 h. The cells were then incubated with primary antibody at 4 °C for overnight. The following antibodies were used: rabbit anti-NANOG (Abcam, # ab80892), rabbit anti-OCT4 (Abcam, # 19857), rabbit anti-SOX2 (Abcam, # ab97959), rabbit anti-PAX6 (Abcam, # ab5790), rabbit anti-SOX2 and mouse anti-NESTIN (Santa Cruz Biotechnology, # sc23927), chicken anti-GFAP (Abcam # ab4674), rabbit anti-S100ß (Abcam, # ab196442), rabbit anti-EAAT-1 (Abcam, # ab416) and mouse anti-GS(Abcam, # ab64613). After washing with PBS three times, cells were further incubated with secondary antibody (1:800 in blocking buffer) for 1 h at RT. The secondary antibodies included Alexa Flour® goat anti-mouse 594 (Thermo Fisher Scientific, # A11005) and Alexa Flour® goat anti-rabbit 488 (Thermo Fisher Scientific, # A11008). The coverslips were mounted using Prolong Diamond Antifade Mountant with DAPI (Thermo Fisher Scientific, # P36962).

4.4. Intracellular ATP production

Intracellular ATP production was detected using the Luminescent ATP Detection Assay Kit (Abcam, # ab113849). Cells were grown to 90% confluency in 96-well plate (Life Sciences, # 3601). ATP measurements were conducted based on manufacturer's protocol. Cells were lysed. Luciferase enzyme and luciferin were added. Emitted light corresponding to the number of ATPs was measured in a Victor® XLight Multimode Plate Reader (PerkinElmer). For each sample, 3–6 replicates were measured. To normalize ATP production by cell numbers, cells grown in the same 96 well plates were stained using Janus Green cell normalization stain kit (Abcam, # ab111622). OD value at 595 nm was measured by Labsystems Multiskan Bichromatic plate reader (Titertek Instruments, USA).

4.5. ROS production

ROS production was measured by flow cytometry. Intracellular ROS production in relation to mitochondrial mass was quantified using double staining of 30 μM DCFDA (Abcam, # ab11385) and 150 nM MTDR (Invitrogen, # M22426). Mitochondrial ROS production in relation to mitochondrial mass was detected using double staining of 10 μM mitochondrial superoxide indicator MitoSOX Red (Thermo Fisher Scientific, # M36008) and 150 nM MTG. The stained cells were detached using TrypLE Express enzyme and neutralized using culture media with 10% FBS, before being analyzed on a FACS BD Accuri™ C6 flow cytometer. More than 40,000 cells were recorded for each sample. Results were analyzed using BD Accuri C6 Software.

4.6. NADH and NAD^+ measurement

NADH and NAD^+ levels were measured using LC-MS. After washing with PBS, cells were incubated with ice-cold 80% methanol for 20 min at 4 °C and were stored at -80 °C overnight. The next day, samples were thawed on a rotating wheel at 4 °C and subsequently centrifuged at 16000*g* for 20 min at 4 °C. The supernatant was added to 1 volume of acetonitrile and were stored at -80 °C until analysis. The cell pellet was dried and reconstituted in lysis buffer (20 mM Tris-HCl (pH 7.4), 2% SDS, 1 mM EDTA, 150 mM NaCl) for protein determination (BCA assay). Metabolite separation was achieved by using a ZIC-pHILC column (150 x 4.6 mm, 5 μm; Merck) and Dionex UltiMate 3000 liquid chromatography system (Thermo Fisher Scientific). The column temperature was kept at 30 °C. The mobile phase consisted of 10 mM ammonium acetate pH 6.8 (Buffer A) and acetonitrile (Buffer B). The flow rate was kept at 400 μL/min, and the gradient was set at 0 min 20% Buffer B, 15-20 min 60% Buffer B, 35 min 20% Buffer B. Ionization was achieved by heated electrospray ionization (HESI-II) probe (Thermo Fisher Scientific) using the positive ion polarity mode, with a spray voltage of 3.5 kV. The sheath gas flow rate was 48 units. The auxiliary gas flow rate was 11 units. The sweep gas flow rate was 2 units. The capillary temperature was 256 °C. The auxiliary gas heater temperature was 413 °C. The stacked-ring ion guide (S-lens) radio frequency level was at 90 units. Mass spectra were recorded by QExactive mass spectrometer (Thermo Fisher Scientific). Data analysis was performed using Thermo Xcalibur Qual Browser (Thermo Fisher Scientific). Standard curves generated for NAD^+ and NADH were used as quantification references.

4.7. Measurement of mtDNA copy number

MtDNA copy number was quantified using both flow cytometry and qPCR. For flow cytometry, cells were double stained with TFAM and TOMM20. Cells were detached with TrypLE Express enzyme and fixed with 1.6% (*v*/v) PFA (VWR, # 100503 917) for 10 min at RT. Thereafter, cells were permeabilized with ice-cold 90% methanol for 20 min at -20 °C, and blocked-in blocking buffer containing PBS, 0.3 M glycine, 5% goat serum and 1% bovine serum albumin (BSA). Cells were incubated with anti-TFAM antibody conjugated to Alexa Fluor® 488 (Abcam, # ab198308) at 1:400 dilutions and anti-TOMM20 antibody conjugated to Alexa Fluor® 488 (Santa Cruz Biotechnology, # sc 17,764 AF488) at 1:400 dilutions. The cells were then analyzed on BD Accuri™ C6 flow cytometer and data analysis was performed using BD Accuri C6 Software. The mtDNA quantities relative to mitochondria mass were

represented by TFAM/TOMM20 ratio.

For qPCR, DNA was extracted using a QIAGEN DNeasy Blood and Tissue Kit (QIAGEN, # 69504) according to the manufacturer's protocol. MtDNA was quantified as previously described (Liang et al., 2021a; Liang et al., 2020c).

4.8. Measurement of complex I, II, and IV expression

Protein levels of mitochondrial complexes I, II, and IV were accessed using flow cytometry. Cells were detached with TrypLE Express enzyme and were fixed with 1.6% (v/v) PFA (VWR, # 100503 917) for 10 min at RT, before permeabilized using ice-cold 90% methanol at -20 °C for 20 min. The cells were blocked using the blocking buffer mentioned above. Cells were stained with primary antibodies at dilutions 1:1000. The primary antibodies include anti-NDUFB10 (Abcam, # ab196019), anti-SDHA (Abcam, # ab14715) and anti-COX IV (Abcam, # ab14744). The secondary antibodies were subsequently incubated at dilutions 1:400. The cells were analyzed on BD Accuri™ C6 flow cytometer and data analysis was performed using BD Accuri C6 Software. At least 40,000 events were recorded for each sample, doublets or dead cells were excluded.

4.9. MMP and mitochondrial mass measurement

MMP relative to mitochondrial mass was measured using flow cytometry. Cells were duel stained with 100 nM TMRE (Abcam, # ab113852) and 150 nM MTG (Invitrogen, # M7514) for 45 min at 37 °C. Cells treated with 100 μM FCCP (Abcam, # ab120081) was used as negative control. After washing with PBS, cells were detached with TrypLE enzyme and neutralized with culture media plus 10% FBS. The cells were then analyzed on a FACS BD Accuri™ C6 flow cytometer (BD Biosciences, San Jose, CA, USA). The data analysis was performed using BD Accuri C6 Software. At least 40,000 events were recorded for each sample, doublets or dead cells were excluded.

4.10. Bulk RNA sequencing analysis

Total RNA was isolated from NSCs and iPSCs using RNeasy Mini Kit (QIAGEN). RNA quality and concentration were checked using Bioanalyzer and Qubit™. RNA sequencing libraries were established by the PolyA enrichment method. For iPSCs and NSCs, sequencing was performed by HudsonAlpha. FASTQ files were trimmed using Trimmomatic version 0.39 to remove potential Illumina adapters and low-quality bases with the following parameters: ILLUMINACLIP: truseq. fa: 2:30:10 LEADING:3 TRAILING:3 SLIDINGWINDOW: 4:15 (Bolger et al., 2014). FASTQ files were assessed using fastQC version 0.11.8 prior and following trimming. We used Salmon version 1.0.0 (Patro et al., 2017) to quantify the abundance at the transcript level with the fragment-level GC bias correction option (*gcBias*flag) and the appropriate option for the library type (*l*flag set to A) against the GENCODE release 32 of the human transcriptome (GRCh38.p13). Transcript-level quantification was imported into R and collapsed onto gene-level quantification using the tximport R package version 1.8.0 (Soneson et al., 2015) according to the gene definitions provided by the same GENCODE release. We filtered out genes in non-canonical chromosomes and scaffolds, and transcripts encoded by the mitochondrial genome. Genes were filtered out if their level of expression was below 10 reads in $>$ 75% of the samples based on counts per million (CPM) (Chen et al., 2016), which resulted in a total of 20,565 genes for downstream analyses. Transcripts counts were aggregated into gene counts. Sample correlations were calculated with the information of DV200, library size, cell type and mutation, and sample outliers were excluded (Fig. S2). Differential expression analysis was conducted using DEseq2 (Love et al., 2014). Multiple comparisons were adjusted by using the false discovery rate method. Adjusted *P* value (q value) $<$0.05 was considered as statistical significance. KEGG pathway and KEGG module enrichment analysis were conducted using Clusterprofiler (Yu et al., 2012). Human MitoCarta 2.0 was used as a reference database of collections of genes with mitochondrial related function and localization (Calvo et al., 2016). For astrocytes, RNA sequencing was performed by Beijing Genomics Institute (BGI, Shenzhen, China). Library preparation was conducted at BGI following the guide of the standard protocol. The sequencing was performed at BGI-Shenzhen using BGISEQ-500. Low-quality reads and adapter contaminated reads were removed using SOAPnuke software (Chen et al., 2018). The processed fastq files were mapped to the human genome using HISAT (Kim et al., 2015). The genome version was GRCh38, with annotations from Bowtie2 (Langmead and Salzberg, 2012). Then the expression level of the gene was calculated by RSEM (v1.2.12) (Li and Dewey, 2011). Differential expression was conducted using the DEseq2 package. Construction of metabolic model and metabolic reporter analysis using RNA sequencing data were conducted as previsouly described (Robinson et al., 2020; Väremo et al., 2015).

4.11. Statistical analysis

All data are expressed as mean ± standard error of the mean (SEM). Statistical analysis was performed using GraphPad Prism 7.0 (GraphPad Software). For a data set that meets the normal distribution, two-side student's *t*-test was applied, otherwise the Mann-Whitney *U* test was applied. *P* values less than 0.05 was considered statistical significance.

Funding

This work was supported by the following funding: K. X. L was partly supported by University of Bergen Meltzers Høyskolefonds (project number:103517133) and Gerda Meyer Nyquist Gulbranson & Gerdt Meyer Nyquist legat (project number: 103816102). L. A. B was supported the Norwegian Research Council (project number: 229652), Rakel og Otto Kr.Bruuns legat. G. J. S was partly supported by the Norwegian Research Council through its Centres of Excellence funding scheme (project number: 262613).

Author's contributions

K.L contribute to the conceptualization; K. X. L, Y. H and C. K. K contribute to the methodology; K. X. L, Y. H, C. K. K, A. C, G. S. N and L. E. H contribute to the investigation; K. X. L and Y. H contribute to the writing original draft; all authors contribute to writing review and editing; K. X. L, L. A. B and G. J. S contribute to the funding acquisition; K. X. L, G. J. S, L. A. B and M. Z contribute to the resources; K. X. L contributes to the supervision. All authors agree to the authorships.

Declaration of Competing Interest

The authors declare that they have no competing interests.

Data availability

The datasets generated and analyzed during the study are included with the Supplemental Information. The RNA sequencing read count data can be accessed in NCBI Gene Expression Omnibus (GEO) data deposit system with an accession number GSE207007. All other data are available from the corresponding author upon request.

Acknowledgements

We thank members of the Molecular Imaging Centre, Flow Cytometry Core Facility for their expertise and assistance in confocal imaging and flow cytometry data recording.

Appendix A. Supplementary data

Supplementary data to this article can be found online at https://doi.org/10.1016/j.expneurol.2023.114429.

References

Bolger, A.M., Lohse, M., Usadel, B., 2014. Trimmomatic: a flexible trimmer for Illumina sequence data. Bioinformatics. 30 (15), 2114–2120.

Calvo, S.E., Clauser, K.R., Mootha, V.K., 2016. MitoCarta2.0: an updated inventory of mammalian mitochondrial proteins. Nucleic Acids Res. 44 (D1), D1251–D1257.

Chan, S.S., Longley, M.J., Copeland, W.C., 2005. The common A467T mutation in the human mitochondrial DNA polymerase (POLG) compromises catalytic efficiency and interaction with the accessory subunit. J. Biol. Chem. 280 (36), 31341–31346.

Chan, S.S., Longley, M.J., Copeland, W.C., 2006. Modulation of the W748S mutation in DNA polymerase gamma by the E1143G polymorphismin mitochondrial disorders. Hum. Mol. Genet. 15 (23), 3473–3483.

Chapman, J., Fielder, E., Passos, J.F., 2019. Mitochondrial dysfunction and cell senescence: deciphering a complex relationship. FEBS Lett. 593 (13), 1566–1579.

Chen, Y., Lun, A.T., Smyth, G.K., 2016. From reads to genes to pathways: differential expression analysis of RNA-Seq experiments using Rsubread and the edgeR quasi-likelihood pipeline. F1000Res. 5, 1438.

Chen, Y., Chen, Y., Shi, C., Huang, Z., Zhang, Y., Li, S., et al., 2018. SOAPnuke: a MapReduce acceleration-supported software for integrated quality control and preprocessing of high-throughput sequencing data. Gigascience. 7 (1), 1–6.

Chen, A., Kristiansen, C.K., Hong, Y., Kianian, A., Fang, E.F., Sullivan, G.J., et al., 2021. Nicotinamide riboside and metformin ameliorate Mitophagy defect in induced pluripotent stem cell-derived astrocytes with mutations. Front. Cell Dev. Biol. 9, 737304.

Chen, A., Kristiansen, C.K., Høyland, L.E., Ziegler, M., Wang, J., Sullivan, G.J., et al., 2022. POLG mutations lead to abnormal mitochondrial remodeling during neural differentiation of human pluripotent stem cells via SIRT3/AMPK pathway inhibition. Cell Cycle 1-16.

Correia-Melo, C., Marques, F.D., Anderson, R., Hewitt, G., Hewitt, R., Cole, J., et al., 2016. Mitochondria are required for pro-ageing features of the senescent phenotype. EMBO J. 35 (7), 724–742.

Farnum, G.A., Nurminen, A., Kaguni, L.S., 2014. Mapping 136 pathogenic mutations into functional modules in human DNA polymerase gamma establishes predictive genotype-phenotype correlations for the complete spectrum of POLG syndromes. Biochim. Biophys. Acta 1837 (7), 1113–1121.

Hakonen, A.H., Heiskanen, S., Juvonen, V., Lappalainen, I., Luoma, P.T., Rantamaki, M., et al., 2005. Mitochondrial DNA polymerase W748S mutation: a common cause of autosomal recessive ataxia with ancient European origin. Am. J. Hum. Genet. 77 (3), 430–441.

Janssen, W., Quaegebeur, A., Van Goethem, G., Ann, L., Smets, K., Vandenberghe, R., et al., 2016. The spectrum of epilepsy caused by POLG mutations. Acta Neurol. Belg. 116 (1), 17–25.

Kang, S., Louboutin, J.P., Datta, P., Landel, C.P., Martinez, D., Zervos, A.S., et al., 2013. Loss of HtrA2/Omi activity in non-neuronal tissues of adult mice causes premature aging. Cell Death Differ. 20 (2), 259–269.

Kim, D., Langmead, B., Salzberg, S.L., 2015. HISAT: a fast spliced aligner with low memory requirements. Nat. Methods 12 (4), 357–360.

Kollberg, G., Moslemi, A.R., Darin, N., Nennesmo, I., Bjarnadottir, I., Uvebrant, P., et al., 2006. POLG1 mutations associated with progressive encephalopathy in childhood. J. Neuropathol. Exp. Neurol. 65 (8), 758–768.

Lan, R., Wu, J.T., Wu, T., Ma, Y.Z., Wang, B.Q., Zheng, H.Z., et al., 2018. Mitophagy is activated in brain damage induced by cerebral ischemia and reperfusion via the PINK1/Parkin/p62 signalling pathway. Brain Res. Bull. 142, 63–77.

Langmead, B., Salzberg, S.L., 2012. Fast gapped-read alignment with bowtie 2. Nat. Methods 9 (4), 357–359.

Lax, N.Z., Whittaker, R.G., Hepplewhite, P.D., Reeve, A.K., Blakely, E.L., Jaros, E., et al., 2012. Sensory neuronopathy in patients harbouring recessive polymerase gamma mutations. Brain. 135 (Pt 1), 62–71.

Lee, Y.S., Kennedy, W.D., Yin, Y.W., 2009. Structural insight into processive human mitochondrial DNA synthesis and disease-related polymerase mutations. Cell. 139 (2), 312–324.

Li, B., Dewey, C.N., 2011. RSEM: accurate transcript quantification from RNA-Seq data with or without a reference genome. BMC Bioinformatics 12, 323.

Liang, K.X., Kianian, A., Chen, A., Kristiansen, C.K., Hong, Y., Furriol, J., et al., 2020a. Stem cell derived astrocytes with POLG mutations and mitochondrial dysfunction including abnormal NAD+ metabolism is toxic for neurons. bioRxiv, 2020.12.20.423652.

Liang, X., Kristiansen, C.K., Vatne, G.H., Hong, Y., Bindoff, L.A., 2020b. Patient-specific neural progenitor cells derived from induced pluripotent stem cells offer a promise of good models for mitochondrial disease. Cell Tissue Res. 380 (1), 15–30.

Liang, K.X., Kristiansen, C.K., Mostafavi, S., Vatne, G.H., Zantingh, G.A., Kianian, A., et al., 2020c. Disease-specific phenotypes in iPSC-derived neural stem cells with POLG mutations. EMBO Mol. Med. 12 (10), e12146.

Liang, K.X., Vatne, G.H., Kristiansen, C.K., Ievglevskyi, O., Kondratskaya, E., Glover, J.C., et al., 2021a. N-acetylcysteine amide ameliorates mitochondrial dysfunction and reduces oxidative stress in hiPSC-derived dopaminergic neurons with POLG mutation. Exp. Neurol. 337, 113536.

Liang, K.X., Chen, A., Kristiansen, C.K., Bindoff, L.A., 2021b. Flow cytometric analysis of multiple mitochondrial parameters in human induced pluripotent stem cells and their neural and glial derivatives. J. Visual. Exp. 177.

Love, M.I., Huber, W., Anders, S., 2014. Moderated estimation of fold change and dispersion for RNA-seq data with DESeq2. Genome Biol. 15 (12), 550.

Marcus, J.M., Andrabi, S.A., 2018. SIRT3 regulation under cellular stress: making sense of the ups and downs. Front. Neurosci. 12, 799.

Moiseeva, O., Bourdeau, V., Roux, A., Deschenes-Simard, X., Ferbeyre, G., 2009. Mitochondrial dysfunction contributes to oncogene-induced senescence. Mol. Cell. Biol. 29 (16), 4495–4507.

Patro, R., Duggal, G., Love, M.I., Irizarry, R.A., Kingsford, C., 2017. Salmon provides fast and bias-aware quantification of transcript expression. Nat. Methods 14 (4), 417–419.

Rahman, S., Copeland, W.C., 2019. POLG-related disorders and their neurological manifestations. Nat. Rev. Neurol. 15 (1), 40–52.

Robinson, J.L., Kocabaş, P., Wang, H., Cholley, P.-E., et al., 2020. An atlas of human metabolism. Sci. Signal. 13, eaaz1482. https://doi.org/10.1126/scisignal.aaz1482.

Shi, R.Y., Zhu, S.H., Li, V., Gibson, S.B., Xu, X.S., Kong, J.M., 2014. BNIP3 interacting with LC3 triggers excessive mitophagy in delayed neuronal death in stroke. CNS Neurosci. Ther. 20 (12), 1045–1055.

Soneson, C., Love, M.I., Robinson, M.D., 2015. Differential analyses for RNA-seq: transcript-level estimates improve gene-level inferences. F1000Res. 4, 1521.

Song, S., Lam, E.W., Tchkonia, T., Kirkland, J.L., Sun, Y., 2020. Senescent cells: emerging targets for human aging and age-related diseases. Trends Biochem. Sci. 45 (7), 578–592.

Tzoulis, C., Engelsen, B.A., Telstad, W., Aasly, J., Zeviani, M., Winterthun, S., et al., 2006a. The spectrum of clinical disease caused by the A467T and W748S POLG mutations: a study of 26 cases. Brain. 129 (Pt 7), 1685–1692.

Tzoulis, C., Engelsen, B.A., Telstad, W., Aasly, J., Zeviani, M., Winterthun, S., et al., 2006b. The spectrum of clinical disease caused by the A467T and W748S POLG mutations: a study of 26 cases. Brain. 129 (7), 1685–1692.

Tzoulis, C., Tran, G.T., Schwarzlmuller, T., Specht, K., Haugarvoll, K., Balafkan, N., et al., 2013. Severe nigrostriatal degeneration without clinical parkinsonism in patients with polymerase gamma mutations. Brain. 136 (Pt 8), 2393–2404.

Tzoulis, C., Tran, G.T., Coxhead, J., Bertelsen, B., Lilleng, P.K., Balafkan, N., et al., 2014a. Molecular pathogenesis of polymerase gamma-related neurodegeneration. Ann. Neurol. 76 (1), 66–81.

Tzoulis, C., Tran, G.T., Coxhead, J., Bertelsen, B., Lilleng, P.K., Balafkan, N., et al., 2014b. Molecular pathogenesis of polymerase γ-related neurodegeneration. Ann. Neurol. 76 (1), 66–81.

Väremo, L., Scheele, C., Broholm, C., Mardinoglu, A., Kampf, C., Asplund, A., et al., 2015. Proteome- and transcriptome-driven reconstruction of the human myocyte metabolic network and its use for identification of markers for diabetes. Cell. Rep. 11 (6), 921–933.

Wang, Y., Nartiss, Y., Steipe, B., McQuibban, G.A., Kim, P.K., 2012. ROS-induced mitochondrial depolarization initiates PARK2/PARKIN-dependent mitochondrial degradation by autophagy. Autophagy. 8 (10), 1462–1476.

Yu, G., Wang, L.G., Han, Y., He, Q.Y., 2012. clusterProfiler: an R package for comparing biological themes among gene clusters. OMICS. 16 (5), 284–287.